

Original Paper

Differential adsorption characteristics in the composite model of deep marine shale: Implication from molecular dynamics simulations

Yu-Ying Wang ^a, Jun-Qing Chen ^{a, b, *}, Fu-Jie Jiang ^c, Xiao-Bin Yang ^a, Xiao Zhang ^a,
Hong Pang ^c, Dong-Xia Chen ^c, Bing-Yao Li ^a, Xin-Yi Niu ^a, Gui-Li Ma ^a, Kan-Yuan Shi ^c

^a Collage of Science, China University of Petroleum (Beijing), Beijing, 102249, China

^b Beijing Key Laboratory of Optical Detection Technology for Oil and Gas, China University of Petroleum (Beijing), Beijing, 102249, China

^c Collage of Geosciences, China University of Petroleum (Beijing), Beijing, 102249, China

ARTICLE INFO

Article history:

Received 6 September 2024

Received in revised form

20 November 2024

Accepted 13 March 2025

Available online xxx

Edited by Jie Hao

Keywords:

Adsorption mechanisms

Kerogen model

Longmaxi formation

Marine shale molecular simulation

Shale gas

ABSTRACT

Shale gas serves as a significant strategic successor resource for future oil and gas reserves and production in China. Thus, a profound understanding of the adsorption mechanism of shale gas in shale reservoirs is crucial to accurately predict and evaluate shale gas reserves. In this study, we utilized two simulation methods, molecular dynamics simulation and Giant Canonical Monte Carlo simulation to examine the adsorption characteristics of kerogen under varying temperature and pressure conditions. We compared the results under identical temperature and pressure conditions for different mineral–kerogen composite models. Moreover, we examined the effects of temperature, pressure, and mineral species on the kerogen adsorption mechanism. The results indicate that shale formations with high organic matter content and a substantial proportion of non-clay inorganic minerals, as well as those subjected to higher temperature and pressure conditions than the shallow layer, possess a greater capacity to accommodate shale gas. This study examined the adsorption mechanism of methane in shale gas using different mineral–kerogen composite models. The findings of this study provide more accurate guidance and support for efficient development of shale gas.

© 2025 The Authors. Publishing services by Elsevier B.V. on behalf of KeAi Communications Co. Ltd. This is an open access article under the CC BY license (<http://creativecommons.org/licenses/by/4.0/>).

1. Introduction

Shale gas is a type of unconventional natural gas found in organic-rich shale formations. The global geological reserves of shale gas are estimated to be 10^{14} m³, with a recoverable resource of 2.43×10^{14} m³ (Energy Information Administration). As of 2021, China's proven shale gas reserves amount to 2.18×10^{13} m³, indicating significant potential. Despite possessing diverse shale types and a complex geological environment, the development of shale gas in China is at a relatively early stage, necessitating further research (Zhang, 2013; Yan et al., 2013; Wang et al., 2021a). Shale gas primarily exists as adsorbed gas, comprising between 20% and 85% of its composition (Curtis, 2002). Thus, investigating the adsorption mechanisms of shale gas is crucial to accurately predict shale gas reserves and improve shale gas recovery and production.

Currently, prevalent research methods include experimental

approaches and molecular simulations. Owing to the prevalence of adsorbed gas within the micro- and nano-pores of shale gas kerogen, experimental conditions often result in the loss of light hydrocarbons. In addition, the increased heterogeneity of shale poses challenges in characterizing the impact of individual mineral. This limitation impedes the microscopic understanding of the shale gas adsorption mechanisms. Molecular simulation methods offer a solution by studying shale gas adsorption mechanisms at the molecular level. This approach facilitates the analysis of factors, such as pressure and temperature, and their effects on the adsorption characteristics of shale gas within the kerogen matrix.

Nan et al. (2020) utilized graphene as an adsorbent for organic matter to investigate the impact mechanisms of different pore sizes and temperature–pressure conditions on methane adsorption in shale. Liu et al. (2016) replaced shale pores with graphene slit structures to investigate methane adsorption in shale pores and analyzed the density distribution of CH₄ in slits of varying sizes and temperatures. However, their study did not quantitatively characterize the adsorption quantity. Graphene, characterized by its hexagonal honeycomb layer structure of carbon atoms, constitutes

* Corresponding author. Collage of Science, China University of Petroleum, Beijing, China.

E-mail address: cjq7745@163.com (J.-Q. Chen).

a single-element composition and cannot represent the complexity of the organic matter structure in shale. Organic matter in shale primarily comprises of kerogen Tissot et al. (1974), which is categorized into three types: Type I, sapropelic kerogen, obtained from the accumulation of algal matter; Type II, mixed kerogen, is derived from planktonic organisms; and Type III, humic kerogen, is primarily sourced from terrestrial higher plants. Given its complex and unstructured composition, accurately describing the molecular-scale structure of kerogen is a crucial.

Domestic research has been undertaken on the development of kerogen models and the adsorption of shale gas within the organic matter of kerogen (Zhang et al., 2012; Wang et al., 2015, 2018). Katti et al. (2017) developed a comprehensive three-dimensional kerogen model comprising seven two-dimensional structures. Previous studies utilized a combination of elemental analysis experiments, solid-state nuclear magnetic resonance experiments, Fourier-transform infrared spectroscopy experiments, and X-ray photoelectron spectroscopy experiments to characterize the molecular structure of kerogen organic matter. They investigated the effect of different slit pore sizes on methane adsorption by kerogen (Hou et al., 2023; Shi et al., 2024; Wang et al., 2019). Ambrose et al. (2011) discovered that shale pore volume differed from free gas volume, indicating that shale gas adsorption conformed to Langmuir theory (single-molecule adsorption theory). Chen et al. (2016) analyzed temperature variations, and examined the effect of pressure changes and water content on the surface of pores on CH₄ adsorption. They observed that the presence of water on the slit surface reduced adsorption effectiveness. Xu et al. through molecular simulation, found variations in the adsorption capacities of different minerals: kerogen exhibited greater adsorption compared to clay minerals and quartz (Xu et al., 2020). This difference arises from the distinct adsorption site characteristics (adsorbate density and adsorption strength) of mineral surfaces.

By summarizing previous research findings, it becomes evident that molecular simulation techniques are widely applied within the petroleum domain. However, a notable gap exists in the literature regarding the differential adsorption characteristics of shale gas across various inorganic mineral–composite kerogens. In this study, we utilized a model representing the organic portion of the Type II kerogen sourced from the marine deep-layer Longmaxi Formation in the Sichuan Basin. The predominant inorganic minerals present in the shale in this region include montmorillonite, kaolinite, illite, quartz, calcite, feldspar, and chlorite. These seven minerals were selected to constitute the inorganic components, thereby creating kerogen–mineral composite models. This approach, which incorporates actual shale components, offers a more authentic representation of a realistic shale structure compared to the utilization of graphite as the organic component. Molecular dynamics simulation (MD) and Giant Canonical Monte Carlo simulation (GCMC) were employed to investigate the adsorption characteristics of the kerogen–mineral composite models. This study aimed to reveal the impact mechanisms of temperature, pressure, and inorganic mineral types on the adsorption of shale gas by kerogen within shale formations.

2. Model construction

2.1. Kerogen structure construction

This study employed kerogen extracted from the Lower Silurian Longmaxi Formation shale from the Lower Ordovician of the Sichuan Basin (Liu et al., 2017). The fundamental structural characteristics of kerogen were analyzed through isothermal adsorption, elemental analysis, X-ray diffraction, Fourier-transform infrared spectroscopy, and ¹³C nuclear magnetic resonance

experiments. The resultant authentic molecular structure model of the kerogen with a molecular formula of C₂₀₆H₁₅₈O₁₉N₄S₄ is shown in (Fig. 1).

Based on micro-component testing, the kerogen in this region was verified to be Type II kerogen. Ten kerogen molecules were selected to construct a periodic box of Type II kerogen with a density of 1.107 g/cm³, which was consistent with the actual density (Zhang et al., 2012). The resulting periodic box with dimensions of 37.4 Å × 37.4 Å × 57.4 Å is illustrated in (Fig. 2). The pore type employed in this study is a slit pore with a fixed pore diameter of 4 nm, as shown in (Fig. 3). Parameter H represents the distance between the upper and lower surfaces of the kerogen that constitutes the pore. The methane (CH₄) molecule model, shown in (Fig. 4), has a bond length of 0.1099 nm and bond angle of 109.471° (Chen et al., 2023a).

2.2. Construction of kerogen–inorganic mineral composite model

The relative composition of shale minerals in the Longmaxi Formation of the Sichuan Basin, is shown in (Fig. 5) (Pan et al., 2022). Notably, the clay minerals primarily comprise of illite, kaolinite, chlorite, and montmorillonite, with illite being the dominant component, ranging from 35.5% to 70.0% and averaging 52.5% (Chen et al., 2023b), as shown in (Fig. 6). Based on these geological conditions, this study selected seven inorganic minerals, including kaolinite, illite, montmorillonite, calcite, chlorite, quartz, and feldspar, to construct a kerogen–inorganic mineral composite shale model.

The crystal cell structures of the seven inorganic minerals were constructed using the Materials Studio 2020 software. The specific parameters of the single-cell models for the inorganic minerals are listed in (Table 1). Montmorillonite belongs to the dioctahedral smectite group and is characterized by its layered silicate composition with a 2:1 type layer structure. It comprises of two layers of silica tetrahedra separated by a layer of silica octahedra. The tetrahedral and octahedral layers are connected by shared oxygen atoms (Gong et al., 2024; Shi et al., 2023). The crystal cell

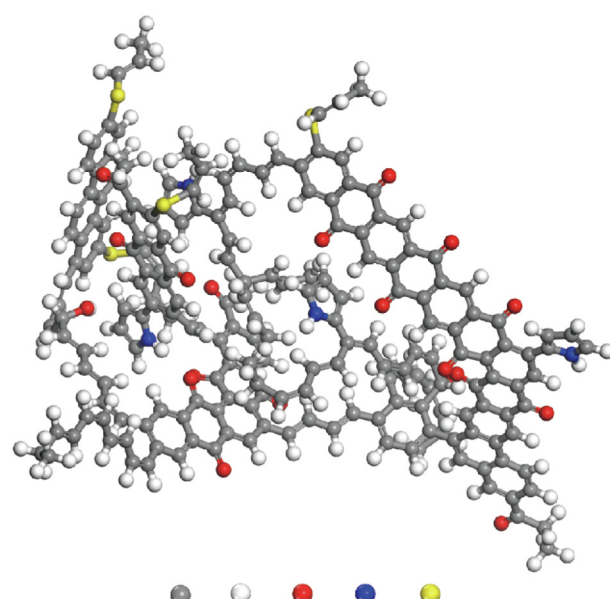


Fig. 1. Three-dimensional molecular structure of type II kerogen shale in the Longmaxi Formation in the Sichuan Basin (C₂₀₆H₁₅₈O₁₉N₄S₄) (The gray spheres represent carbon atoms, white spheres represent hydrogen atoms, red balls represent oxygen atoms, blue balls represent nitrogen atoms, and yellow balls represent sulfur atoms).

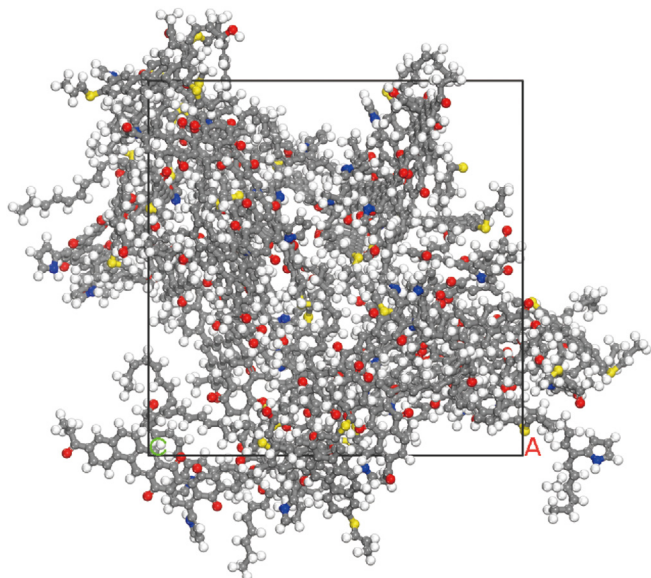


Fig. 2. A periodic box containing 10 kerogen molecules.

parameters were derived from the montmorillonite model developed by Viani (Alberto et al., 2015). Kaolinite, categorized as a 1:1 type octahedral layered silicate, features interlayer connections facilitated by van der Waals force and hydrogen bonding. Notably, the interlayer is devoid of cations and water molecules, and the single unit cell comprises only one structural unit layer, with a single unit cell structure formula of $\text{Al}_4[\text{Si}_4\text{O}_{10}] (\text{OH})_8$ (Bish, 1993). Illites, primary inorganic clay minerals, are composed of two layers of silica tetrahedra with an octahedral layer interposed between them. The tetrahedral layers exhibited isomorphic substitution, where one of every eight Si atoms on one side of the tetrahedra was replaced by an Al atom. This substitution generated a negative charge, which was balanced by the interlayer K^+ ions that stabilized the layers. The crystal cell parameters of illite were obtained from the American Mineralogist Crystal Structure Database, and the model constructed by Dawn et al. (2014). Its molecular structural

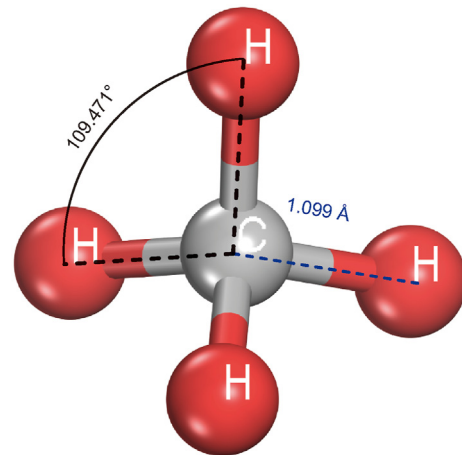


Fig. 4. Optimized methane molecular model.

formula was $\text{K}(\text{Si}_7\text{Al}) \text{Al}_4\text{O}_4(\text{OH})_4$. Chlorite exhibited a 2:1 layered structure, with an interlayer of octahedral hydroxide ions balancing the negative charge of the crystal layers. The crystal cell parameters for chlorite were derived from the American Mineralogist Crystal Structure Database, and the model constructed by Zanazzi et al. (2007). Calcite, a calcium carbonate mineral, has the structural formula CaCO_3 . The crystal cell parameters for calcite were obtained from the American Mineralogist Crystal Structure Database, and the model was constructed by Markgraf et al. (1985). α -quartz comprised silicon dioxide and belonged to the trigonal crystal system. The crystal cell parameters for α -quartz were derived from the model constructed by Antao et al. (2008). Feldspar exhibited a tetrahedral structure with four oxygen atoms surrounding a silicon or aluminum atom. Every two tetrahedra share one oxygen atom, thereby forming a three-dimensional framework. The crystal cell parameters for feldspar were obtained from the American Mineralogist Crystal Structure Database, and the model was constructed by Piera et al. (Piera et al., 1999). The single-cell structures of the seven inorganic minerals were cut along crystal faces using the build-surfaces-cleave surface module, expanded using the build-

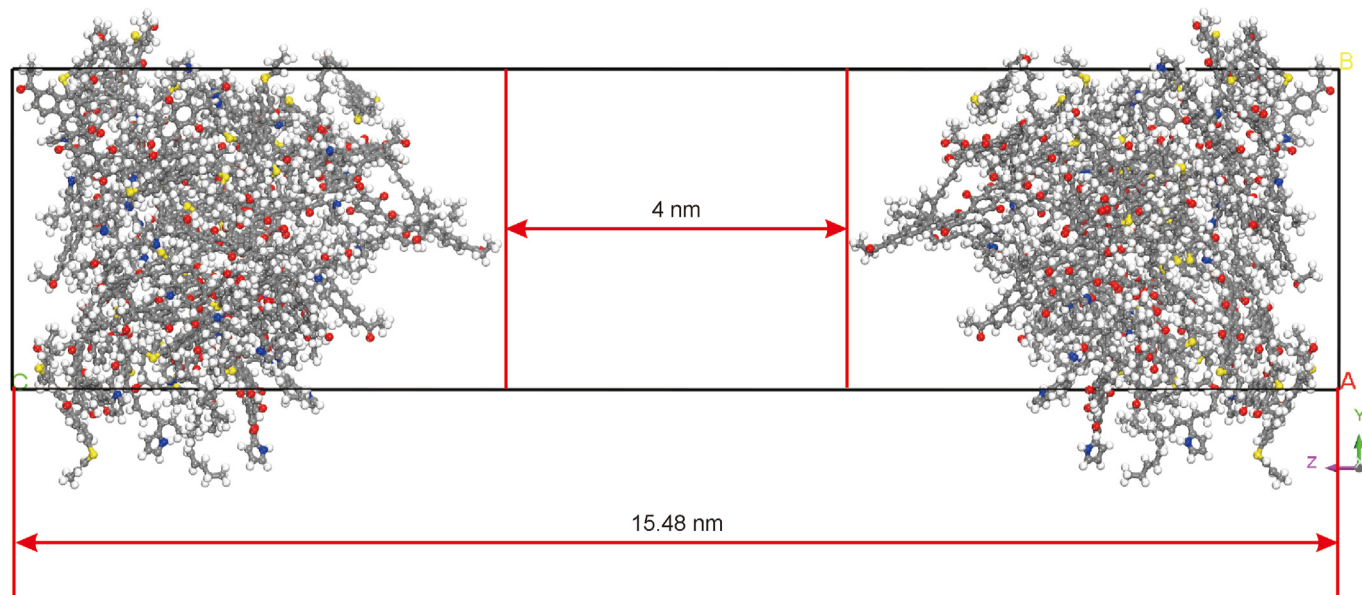


Fig. 3. 4 nm slit pore model of two layers of kerogen organic matter.

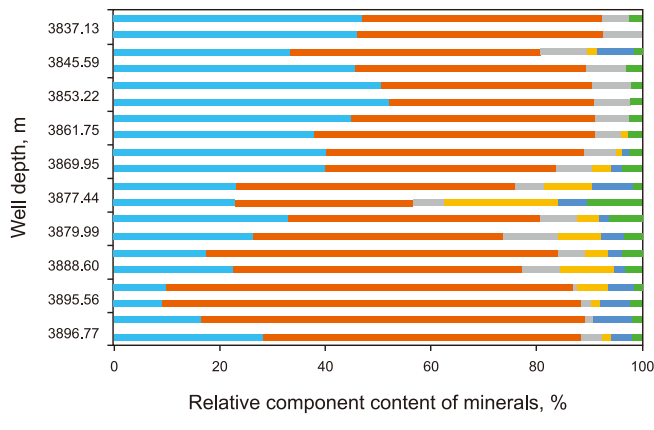


Fig. 5. Relative composition of shale minerals in the Longmaxi Formation of the Sichuan Basin.

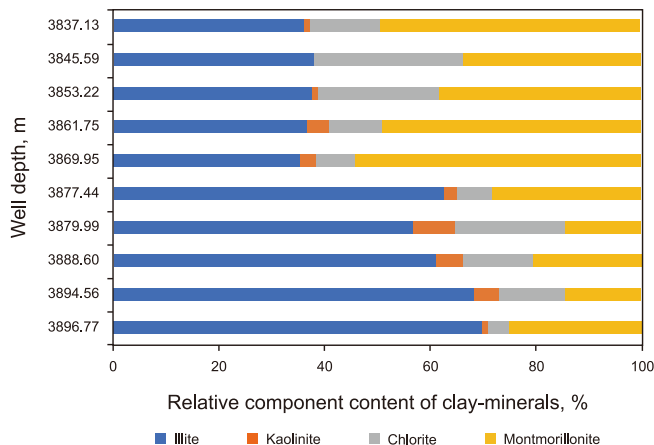


Fig. 6. Relative composition of clay minerals in the Longmaxi Formation shale of the Sichuan Basin.

symmetry-supercell module, and finally underwent geometric optimization and relaxation using the Forcite module. The resulting final configurations are illustrated in (Fig. 7).

Composite configurations of kerogen organic matter were generated by combining kerogen with each of the seven inorganic minerals. Seven composite slit models were developed, namely, Kaolinite-kerogen Type II, Montmorillonite-kerogen Type II, Illite-kerogen Type II, Chlorite-kerogen Type II, Calcite-kerogen Type II, Quartz-kerogen Type II, and Feldspar-kerogen Type II. The pore size of the slit was set at 4 nm. The final configurations, obtained through geometric optimization and relaxation, are shown in Fig. 8.

Table 1
Specific parameters of the single-cell models for inorganic minerals.

Minerals	a, Å	b, Å	c, Å	α_s , °	β_s , °	γ_s , °
Montmorillonite	5.18	8.98	15.00	90.00	99.00	90.00
Illite	5.20	8.97	10.23	90.00	101.57	90.00
Kaolinite	5.15	8.93	7.38	91.90	105.04	89.79
Chlorite	5.225	9.058	28.38	90.00	93.67	90.00
Calcite	4.99	4.99	17.06	90.00	90.00	120.00
Quartz	4.91	4.91	5.40	90.00	90.00	120.00
Feldspar	8.33	12.97	7.14	90	115.6	90

3. Simulation details

3.1. Calculation method

In this study, Materials Studio 2020 software was used to conduct research using two distinct methods: MD and GCMC. The adsorption capacities of various models for methane were characterized through simulation and calculation of parameters, including the absolute adsorption capacity, adsorption heat, adsorption energy, radial distribution function, and density distribution.

(1) Fugacity, a crucial concept in chemical thermodynamics, represents the effective pressure of a real gas. At low pressures, the difference between fugacity and pressure was small, whereas at high pressures, the fugacity gradually diverged from pressure. Considering that the effective pressure of a real gas must replace the conventional pressure to align with the actual formation conditions, the Peng-Robinson equation of state (Stryjek and Juan, 1986; Cong et al., 2022) was:

$$p = RT/(V_m - b) - a\varphi(T)/[V_m(V_m + b) + b(V_m - b)] \quad (1)$$

$$a = 0.45724R^2T_c^2/P_c \quad (2)$$

$$b = 0.07780RT_c/P_c \quad (3)$$

$$\varphi(T) = [1 + k(1 - T_r^{0.5})]^2 \quad (4)$$

$$k = 0.37464 + 1.54226\eta - 0.26992\eta^2 \quad (5)$$

$$T_r = T/T_c \quad (6)$$

$$\ln \delta = \tau - 1 - \ln(\tau - \varepsilon) - \mu/2\sqrt{2\varepsilon} \ln \left\{ \left[\tau + (1 + \sqrt{2})\varepsilon \right] / \left[\tau + (1 - \sqrt{2})\varepsilon \right] \right\} \quad (7)$$

$$\varepsilon = bp/RT \quad (8)$$

$$\mu = a\varphi(T)p/R^2T^2 \quad (9)$$

where p is the pressure, Pa; T_c is the critical temperature, K; P_c is the critical pressure, Pa; T_r is the contrast temperature, K; η is an eccentricity factor; δ is the fugacity coefficient; τ is the deviation factor. The aforementioned formula was programmed and calculated using MATLAB software to determine the fugacity of methane gas. Fig. 9 shows the fugacity of methane at varying temperatures. As the pressure increases, the fugacity gradually deviates from the pressure, while with increasing temperature, the fugacity of methane increases.

(2) Excess adsorption capacity, as determined by GCMC simulation, represents the absolute adsorption capacity of the gas (Huang et al., 2017):

$$N^\alpha = N_{\max}^\alpha [bp/(1 + bp)] \quad (10)$$

where N^α is the absolute adsorption capacity; N_{\max}^α is the maximum adsorption capacity of Langmuir; p is the pressure; b is the Langmuir constant. The adsorption results obtained in the experiment represent the excess adsorption capacity, which must be calculated for comparison with the experimental results (Sudibandriyo et al., 2003). The excess adsorption capacity was

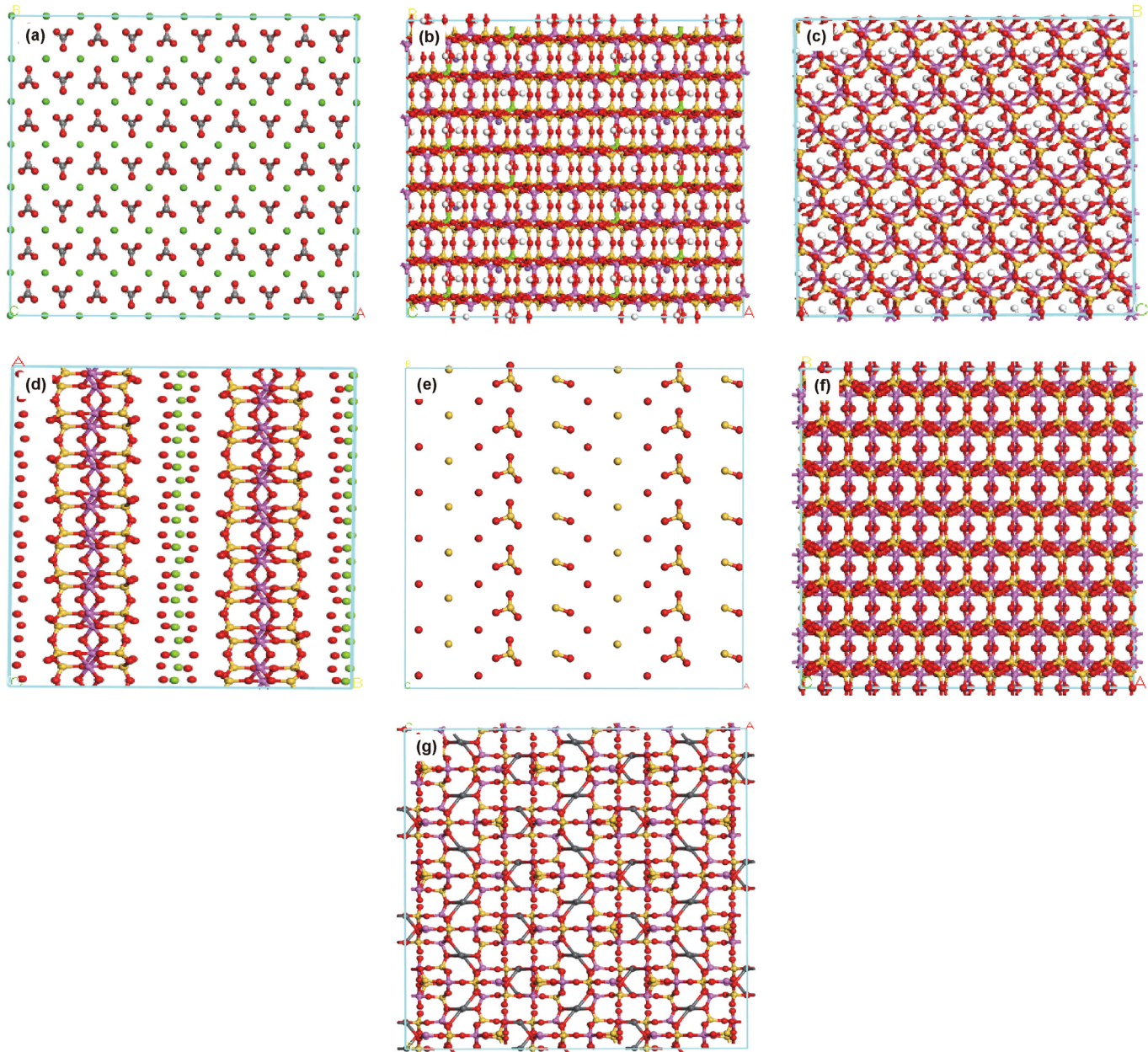


Fig. 7. Presents the three-dimensional structures of the inorganic mineral models. (a) Calcite, (b) montmorillonite, (c) kaolinite, (d) chlorite, (e) quartz, (f) illite, (g) feldspar.

calculated as follows:

$$N^{\alpha} = N^{\alpha} - \rho V_a / M \quad (11)$$

Among them, N^{α} is the excess adsorption capacity, mmol/g; ρ is the density of the gas adsorption phase kg/m³; V_a is the adsorption volume, m³/kg; M is the molar mass of the gas kg/mol (The adsorption capacity mentioned below is all excess adsorption).

(3) Heat of adsorption: When a substance is adsorbed, its kinetic energy decreases and heat is released. The amount of heat released can indicate the adsorption capacity of the mineral for the substance. The larger the adsorption heat, the stronger the adsorption capacity. The conversion equation between the adsorption heat Q^{st} and Henry Changshu H (Shi et al., 2021) was as follows:

$$\ln H = -Q^{\text{st}} / RT + C \quad (12)$$

where Q^{st} is the heat of adsorption of the substance, and H is the Henry constant.

(4) Adsorption energy: By calculating the adsorption energy, we analyzed the ease of adsorption of the adsorbate on the surface model and assessed the relative stability of adsorption. A negative adsorption energy indicated that the adsorption process released energy, indicating that the adsorbate could spontaneously adsorb on the mineral surface. The adsorption energy was calculated as follows (Fang et al., 2022):

$$E^{\text{ads}} = E^{\text{total}} - (E^{\text{sur}} + E^{\text{ab}}) \quad (13)$$

where E^{ads} is the adsorption energy of the system; E^{total} total energy of the system after adsorption; E^{sur} represents the energy of the adsorbed matrix surface before adsorption; E^{ab} denotes the energy of the adsorbed gas before adsorption.

(5) The radial distribution function describes the change in

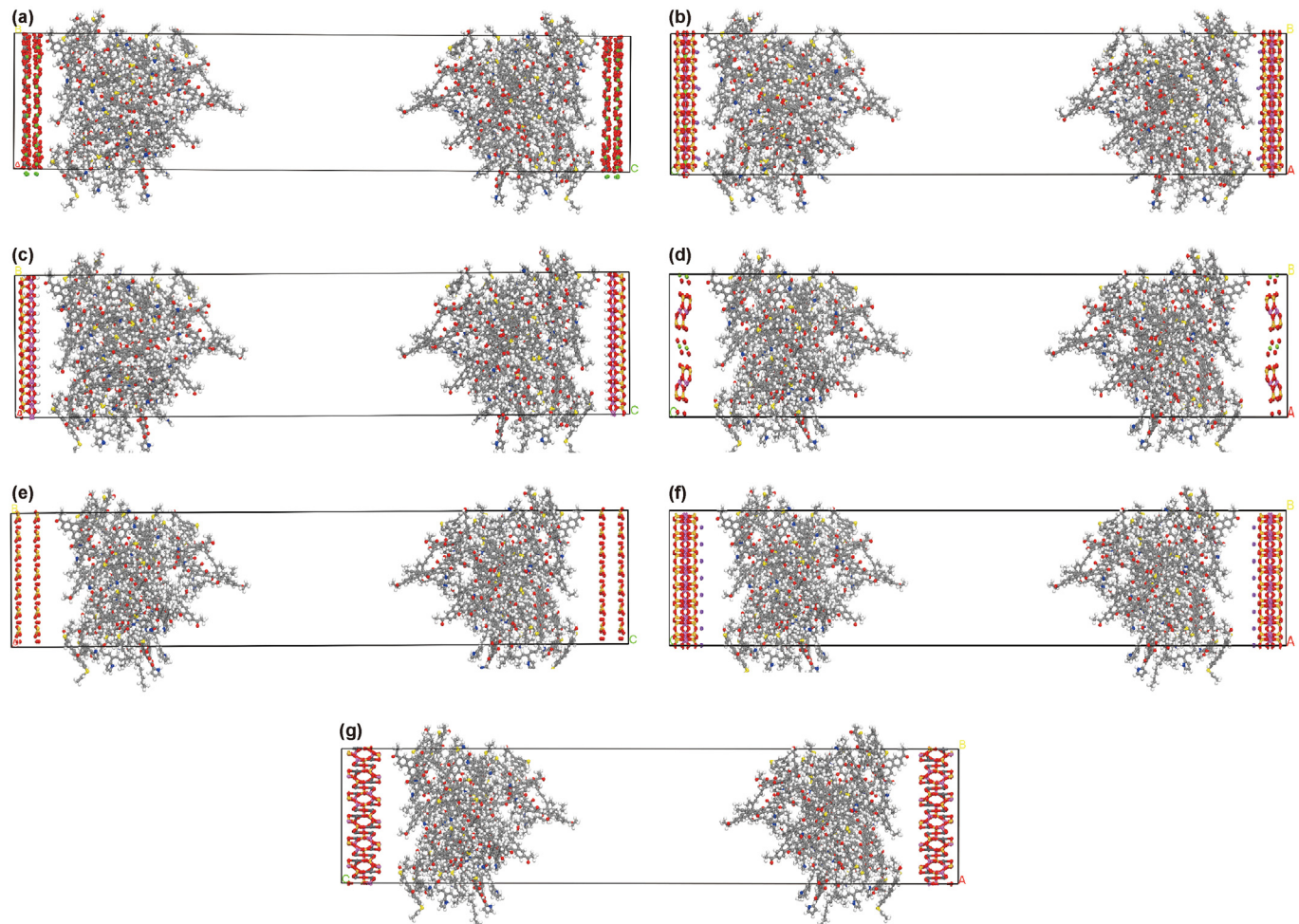


Fig. 8. Three-dimensional composite models of kerogen with inorganic minerals. **(a)** Calcite-kerogen composite model, **(b)** montmorillonite-kerogen composite model, **(c)** kaolinite-kerogen composite model, **(d)** chlorite-kerogen composite model, **(e)** quartz-kerogen composite model, **(f)** illite-kerogen composite model, **(g)** feldspar-kerogen composite model.

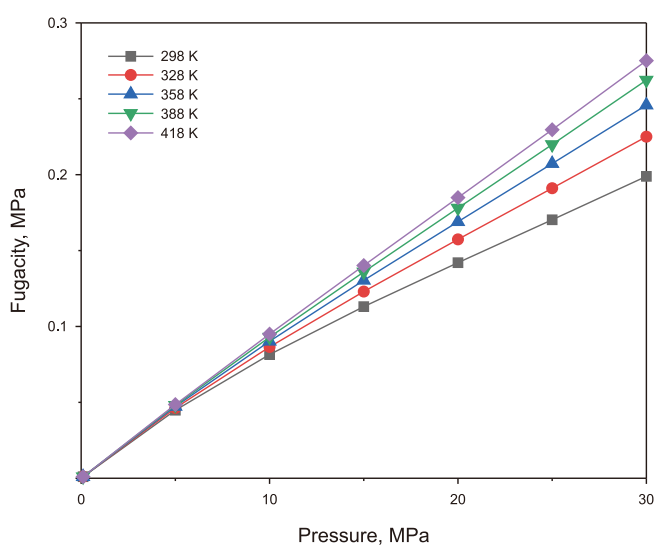


Fig. 9. The fugacity of methane at different temperatures as a function of pressure.

particle density as a function of distance from the reference atom, which can be utilized to characterize the interaction force between two atoms (Liu et al., 2023),

$$g_{ab}(r) = \rho_{ab}(r)V/N_b \quad (14)$$

where $\rho_{ab}(r)$ is defined as the number density of the calculated group of particles in the sphere at r from the reference atom, and the denominator is the average number density of the calculated group of particles.

(6) Density distribution: Adsorbate molecules tend to aggregate heterogeneously at both ends of the pore walls. The density distribution of the adsorbate can characterize the distribution of the adsorbate molecules in pores (Zhou et al., 2023). The results of the MD provide the relative concentrations $R(z)$, where the density of the adsorbate molecules in the pores is:

$$\rho = M \cdot n \cdot R(z) / V \cdot N_A \quad (15)$$

where M is the molar mass of the adsorbate molecule; n is the number of adsorbate molecules; V is the system volume; N_A is Avogadro constant.

3.2. Simulate process

GCMC and MD methods were used to investigate the adsorption behavior of methane in the composite model. The adsorption calculations were conducted using the Sorption module of Materials

Studio (2020) software, with “Fixed pressure” selected for Task and “Metropolis” selected for Method. Each simulation comprised a total of 1.1×10^6 steps, with the initial 1×10^5 steps serving as the equilibrium steps and the remaining 1×10^6 steps representing the adsorption simulation steps of the system. The selected force field was the COMPASS force field (Liu et al., 2013). The simulation system utilized periodic boundary conditions, with the summation method of electrostatic force being Ewald and the van der Waals interaction summation method being Atom based. The L-J potential energy cut-off radius was set to 1.87 nm. A total of eight sets of simulated systems were analyzed, comprising a single kerogen system and seven inorganic mineral–kerogen composite systems.

In the simulation, five temperature points were set, 298, 328, 358, 388, and 418 K. In addition, a total of eight pressure points were set, including 0.1, 2, 5, 10, 15, 20, 25, and 30 MPa. For the MD simulation method, the Forcite module was used. The task was set to Dynamics, employing the canonical ensemble, with a simulation duration of 2 ns.

4. Results

4.1. Absolute adsorption capacity

Fig. 10(a) shows the isothermal adsorption curves of a single kerogen system at different temperatures. In the single kerogen system, methane adsorption decreased with increasing temperature and increased with higher pressure, which was consistent with previous studies (Ambrose et al., 2011). In **Fig. 10(b)–(d)**, notable variations are observed in the isothermal adsorption curves and the

difference in adsorption capacity among different mineral composite model systems. Overall, the clay mineral–kerogen composite model demonstrated lower methane adsorption compared to the non-clay mineral–kerogen composite model. Specifically, the illite–kerogen and chlorite–kerogen composite models exhibited slightly higher methane adsorption than the single kerogen system, with minimal differences in adsorption capacity. Conversely, the non-clay mineral–kerogen composite model systems, particularly, demonstrated remarkably higher methane adsorption compared to the single kerogen system. At pressures below 5 MPa, illite, montmorillonite, calcite, chlorite, quartz, and feldspar enhanced kerogen adsorption, whereas kaolinite inhibited kerogen adsorption. However, at pressures exceeding 5 MPa, the illite and chlorite composite models exhibited methane adsorption comparable to that of the single kerogen system, whereas the montmorillonite and kaolinite composite models exhibited lower methane adsorption. In this scenario, montmorillonite and kaolinite served as inhibitors to the kerogen’s methane adsorption. In addition, composite models of quartz, feldspar, and calcite demonstrated enhanced adsorption of methane for shale gas, thereby facilitating kerogen’s methane adsorption. This variation stemmed from differences in the simulated porosity of the shale models, leading to distinct adsorption capacities for different mineral shale models. These findings were consistent with the simulated results obtained by Li et al. (Li, 2020; Li et al., 2021).

4.2. Adsorption heat

The adsorption heat refers to the thermal effects produced during adsorption. When gas molecules approach a solid surface

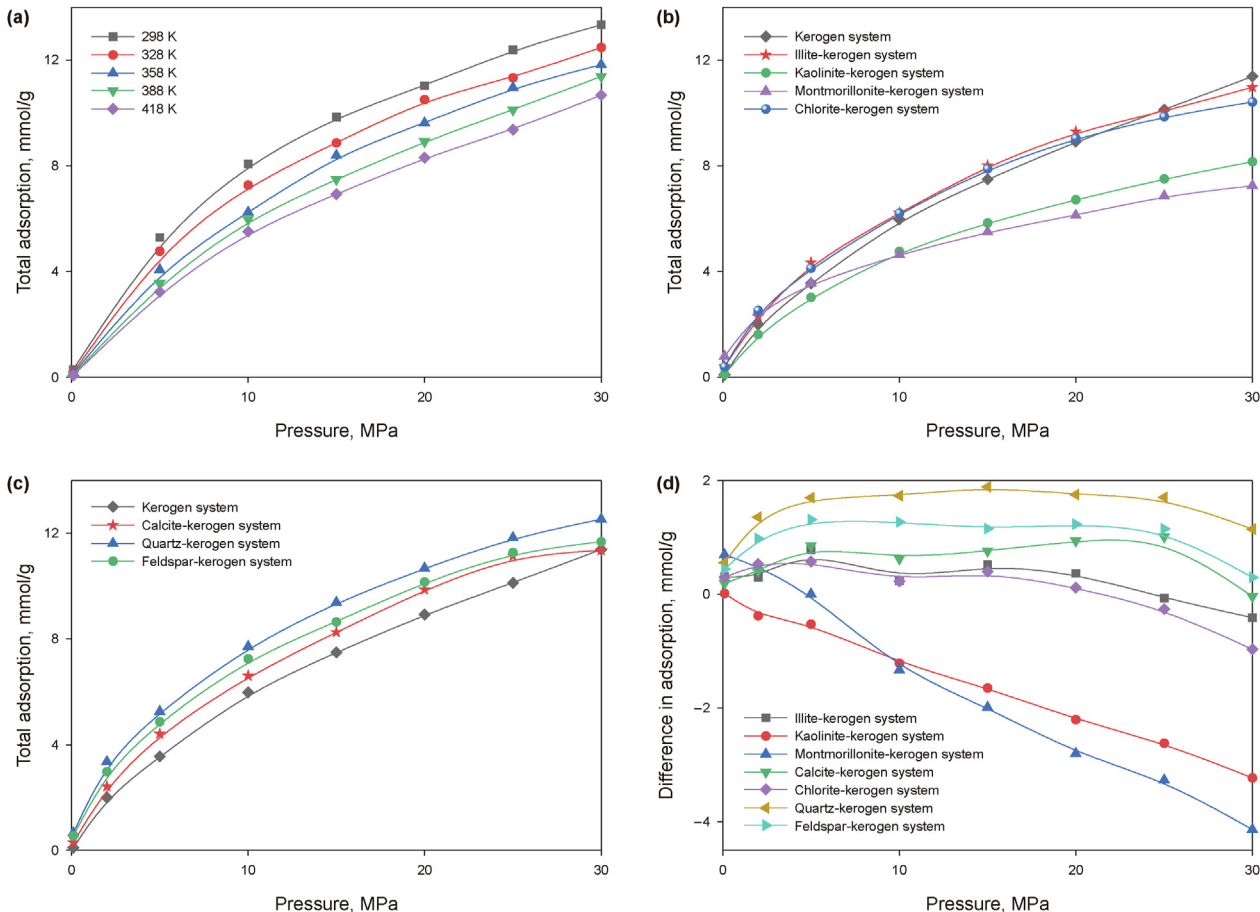


Fig. 10. Isothermal adsorption curves of methane in different systems. **(a)** Kerogen system; **(b)** clay-mineral composite model system; **(c)** non-Clay mineral composite model system; **(d)** difference between the adsorption capacity of methane in different systems and the adsorption capacity of mono kerogen system.

during adsorption, their molecular motion decreases significantly, resulting in heat release. The average adsorption heat range for methane was 8.201 kJ/mol to 30 kJ/mol, which was below 42 kJ/mol, suggesting that methane adsorption in the single kerogen system was primarily attributed to physical adsorption (Chen et al., 2023b). Fig. 11(a) shows the average isothermal adsorption heat curve for a single kerogen system at different temperatures. The average adsorption heat for methane in the single kerogen system decreased with increasing temperature and pressure. During adsorption, as the system temperature increased, the kinetic energy of the methane molecules gradually increased, enhancing Brownian motion. This gradual increase led to a breakthrough of adsorption barriers in the internal surfaces of the pores. The interaction between methane and kerogen molecules weakens in the system, resulting in a decrease in the adsorption heat produced during adsorption, gradually approaching equilibrium (Jia et al., 2023).

Fig. 11(b) shows the adsorption heat for different mineral composite model systems at a temperature of 388 K. The higher adsorption heat observed in the composite models compared to the single kerogen system was attributed to the interactions occurring not only between kerogen and methane within the composite system, but also between inorganic minerals and methane (Wang et al., 2017). Fig. 11(c) and (d) depict the isothermal adsorption heat curves for clay mineral and non-clay mineral composite model systems, respectively, at a temperature of 388 K. The average adsorption heat for methane in the composite systems decreased

with increasing pressure. When the pressure was below 15 MPa, the adsorption heat for the quartz and calcite systems was relatively high, indicating that the adsorption capacities of the quartz and calcite composite models were higher than those of other mineral composite models. The montmorillonite systems exhibited remarkably lower adsorption heat levels than the other composite systems. The analysis of adsorption heat aligned well with the adsorption capacity results.

4.3. Adsorption energy

During the adsorption process, the velocity of molecular motion slows down from fast to slower, ultimately coming to a halt on the surface of the adsorption medium. Due to this reduction in velocity, the system releases a portion of its energy, which is termed as adsorption energy. A negative adsorption energy indicates that the adsorption process is exothermic (Cong, 2023; Wang et al., 2024a,b). A lower adsorption energy indicates that more energy is released during the adsorption, resulting in a lower energy state of system. A system with lower energy is more stable, making the adsorption process more likely to occur, therefore, the adsorption capacity is stronger (Wang et al., 2018, 2024). Fig. 12(a) shows the distribution of adsorption energy for different systems in a single kerogen system under identical temperature conditions. In the single kerogen system, at a constant temperature, the adsorption energy of methane shifted to the right with increasing pressure, signifying that with increasing pressure, methane adsorption

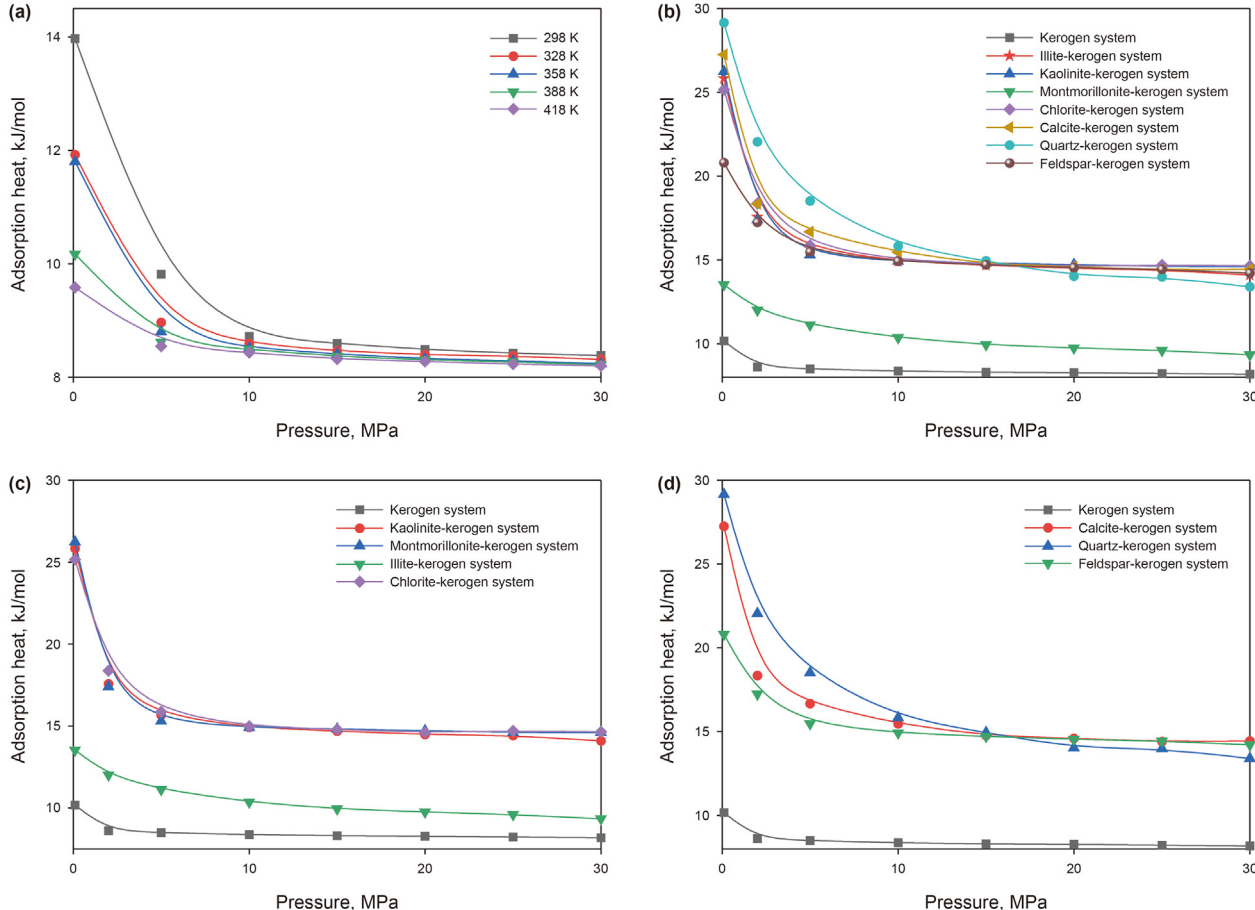


Fig. 11. Average isometric adsorption heat curves of methane under different systems. (a) Kerogen system; (b) composite model systems of different minerals; (c) clay-mineral composite model system; (d) non-clay mineral composite model system

gradually shifted from lower-to higher-energy adsorption sites. Simultaneously, at a constant temperature, the greater the pressure, the stronger the adsorption capacity and stability of a single kerogen system.

Fig. 12(b) shows the distribution of adsorption energy for various mineral composite model systems under identical temperature and pressure conditions. **Fig. 12(c)** and **Fig. 12(d)** show the adsorption energy distribution for clay mineral and non-clay mineral composite model systems, respectively. At a temperature of 388 K and pressure of 15 MPa, the adsorption energy Poisson distribution peaks varied among different composite models. The adsorption energy of the montmorillonite–kerogen composite system was comparable to that of the single kerogen system, whereas the adsorption energy of other systems was remarkably lower than that of the single kerogen system. The adsorption energy distribution for non-clay mineral composite models was left-shifted compared to clay mineral composite models. As shown in **Table 2** and **Fig. 13**, this indicates that, the adsorption capacity and stability are stronger for quartz and calcite composite systems, whereas montmorillonite composite systems exhibit weaker adsorption capacity at constant temperature and pressure. Typically, the adsorption capacity of the clay–mineral composite model was lower than that of the non-clay–mineral composite model. This result was consistent with the adsorption heat and capacity results.

4.4. Radial distribution function

The radial distribution function illustrates how the particle density changes relative to the distance from a reference atom and is used to characterize the interaction forces between two atoms (Li et al., 2022). **Fig. 14(a)** shows the radial distribution functions for methane and individual atoms in a single kerogen system under identical temperature and pressure conditions. The peak values of the radial distribution functions for methane with carbon and sulfur atoms were substantially higher than those observed for other atoms. Compared to nitrogen and oxygen atoms, CH₄ molecules exhibited stronger interactions with carbon and sulfur atoms in kerogen. Consequently, it could be inferred that, under these temperature and pressure conditions, methane selectively adsorbed at the carbon and sulfur atoms in the kerogen. Therefore, it can be inferred that the sites associated with carbon and sulfur atoms served as the primary adsorption sites for methane within this kerogen model (Zhang et al., 2014).

Fig. 14(b) shows the radial distribution functions of the calcite composite model system. The peak radial distribution function value for methane with carbon atoms was the highest, followed by nitrogen and sulfur atoms. This observation suggested that, under identical temperature and pressure conditions, when calcite served as an inorganic interface, the primary adsorption sites for methane are carbon, nitrogen, and sulfur atoms. Calcite, which primarily composed of CaCO₃, formed ionic bonds with the oxygen and calcium atoms. This interaction coupled with the electrostatic effect

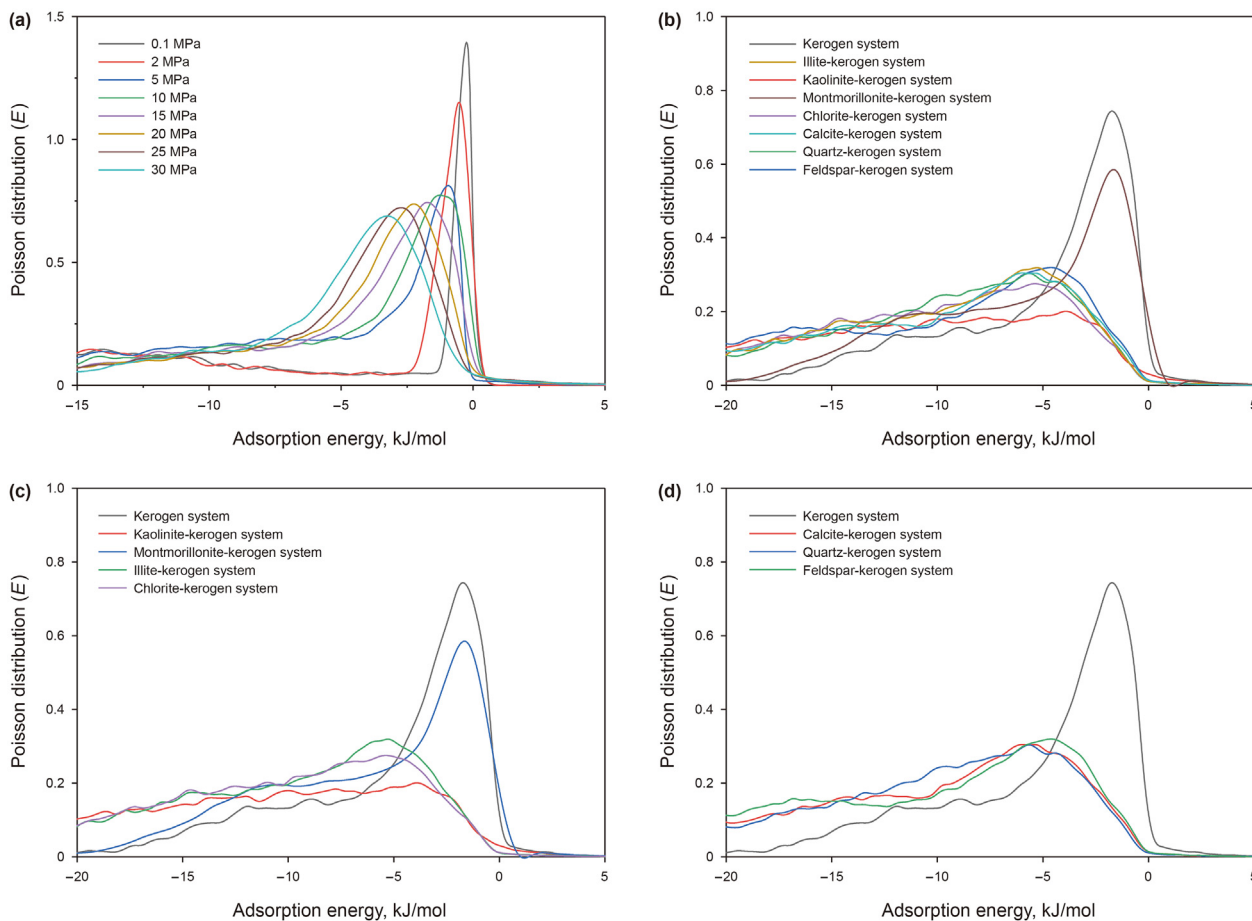


Fig. 12. Adsorption energy distribution curves of methane by different systems at the same temperature. **(a)** Kerogen system; **(b)** composite model systems of different minerals; **(c)** clay-mineral composite model system; **(d)** non-Clay mineral composite model system.

Table 2

Poisson distribution peaks of adsorption energy in different composite models under the same temperature and pressure conditions.

System type	Kerogen	Kaolinite	Montmorillonite	Illite	Chlorite	Calcite	Feldspar	Quartz
Peak Poisson distribution of adsorption energy, kJ/mol	-1.8837	-3.9596	-1.4588	-5.21	-5.1536	-5.3764	-4.376	-5.6268

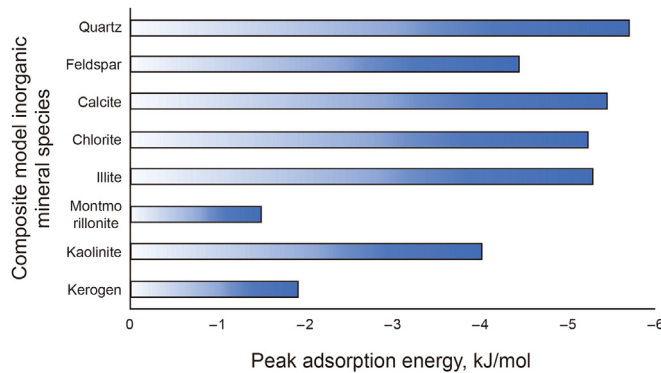


Fig. 13. Peak adsorption energy of different composite models under the same temperature and pressure conditions.

with sulfur atoms in kerogen, resulted in the decreased adsorption of methane molecules (Yuan et al., 2020). The addition of the inorganic mineral calcite did not change the phenomenon of carbon atoms being the primary adsorption sites for methane in the system, as observed in the single kerogen system. This result suggested that, in composite model systems, methane primarily was adsorbed onto the organic matter of kerogen, with the impact of the inorganic mineral calcite on methane adsorption in the system being relatively small.

4.5. Density distribution

Fig. 15(a) shows the density profile along the Z-direction of methane in the narrow slit of the single kerogen system at a pressure of 20 MPa. As shown in the figure, methane was adsorbed in the slit nanopores and within the intrinsic pores of the kerogen. The methane molecules arranged themselves into two symmetrical

adsorption layers in the intrinsic pores of the kerogen to form the main adsorption layer. In addition, a secondary adsorption layer was formed in the middle of the slit nanopores (Gensterblum et al., 2013; Sun et al., 2017). Owing to the macromolecular polymer nature of kerogen organic matter, characterized by various types of bonds interconnected repeatedly and a high degree of branching, complex micro-intrinsic pores were formed within the kerogen substance through spatial torsional stacking. Consequently, during methane adsorption within the system, methane molecules were confined by micropores and were more tightly adsorbed in the micropores of kerogen organic matter (Pang et al., 2019). The weaker adsorbent layer was concentrated in the center of the slit, whereas the methane molecules in other regions were distributed in a free state (Zeng et al., 2018).

Simultaneously, as the temperature increased, the density peak of methane molecules gradually decreased. This finding indicated that with increasing temperature, the adsorption capacity of methane within the pores of kerogen molecules gradually decreased. This finding was consistent with the simulation results of previous studies (Chen et al., 2019; Huang, 2020). For composite model systems, Fig. 15(b) shows the density distribution curves for methane adsorption in the calcite and kaolinite composite model systems. It was evident that distinct density peaks emerged at the edges of the system where inorganic minerals were distributed, within the organic matter of kerogen, and at the central position of the system. This finding suggested that in the mineral–organic composite model, methane adsorption primarily occurred on the organic matter of kerogen, particularly within the inherent pores of kerogen organic matter. The density peak at the central position was attributed to the aggregation of excess adsorbed methane molecules (Hao et al., 2020; Elbashier et al., 2021). Consequently, the adsorption capacity of methane in the calcite–kerogen composite model was significantly higher than in the kaolinite–kerogen composite model. In addition, based on the peak values of the adsorption positions in kerogen, it can be inferred that

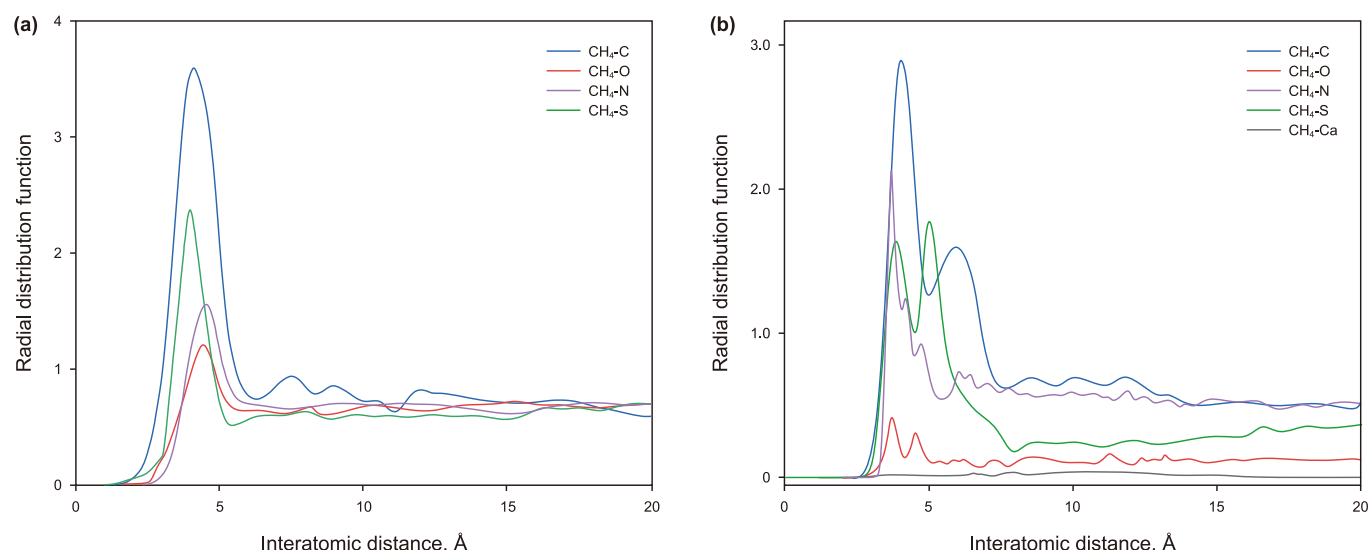


Fig. 14. Radial distribution function between methane and atoms in the system under the same temperature and pressure conditions: (a) Kerogen system; (b) calcite kerogen composite model system.

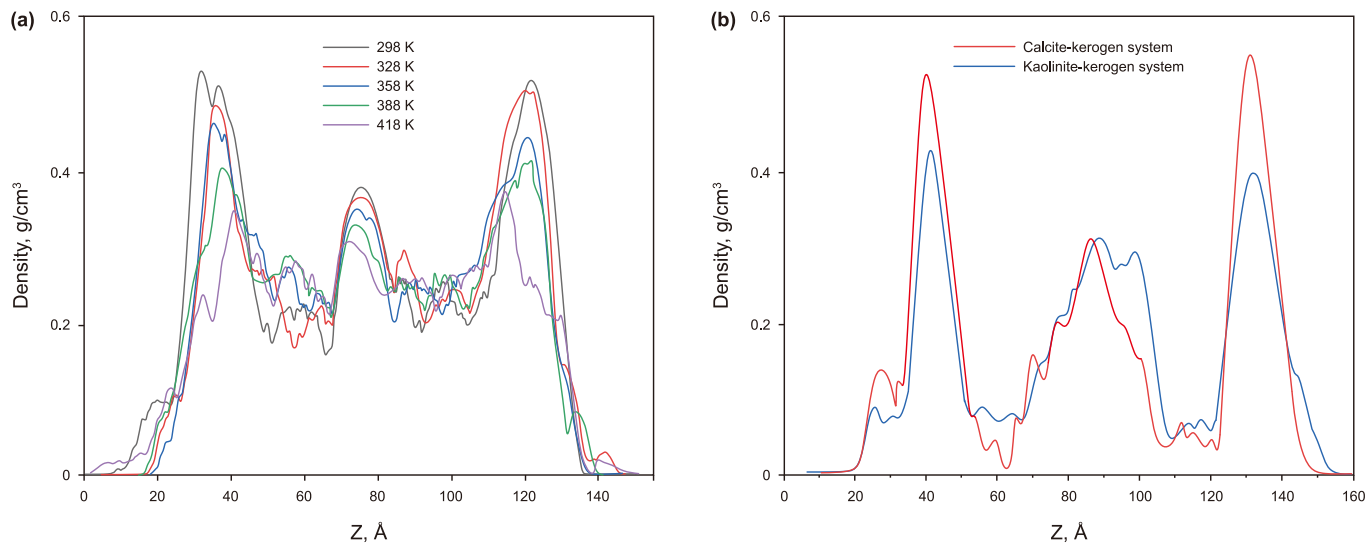


Fig. 15. Density distribution curves in the slits of different methane systems at a constant pressure: (a) Kerogen system; (b) composite model systems of different minerals.

the promotional effect of calcite on methane adsorption in kerogen was higher than that of kaolinite. This finding was consistent with earlier findings.

5. Discussion

5.1. Porosity

Variations in shale model porosity across different systems lead to differences in adsorption results. To determine the porosity of the shale models in this study, we utilized the probe method proposed by Connolly (1983). As illustrated in Fig. 16, molecular volume is defined as the volume of the internal space enclosed by a molecule's surface. When a probe molecule moves along and closely follows the van der Waals surface of the molecule, it produces a purple path as illustrated in Fig. 16. This corresponding surface is termed the Connolly surface, and the volume of the internal space enclosed by it represents the molecular volume (Yang et al., 2017). The probe radius was set to 1.0 Å, and we conducted an estimation of pore sizes in the pre-existing mineral–kerogen composite shale models. The portion of the shale model where the probe atom did not overlap with existing atoms was identified as the free pore volume. Porosity was calculated as the ratio of the free pore volume to the sum of the volumes occupied by the atoms in the shale model and the free pore volume (Sun et al., 2017).

Porosity is the percentage of the pore volume in a bulk material to the total volume of the material in its natural state. It is calculated as follows:

$$p_0 = V_F / (V_0 + V_F) \times 100\% \quad (16)$$

where, V_F is the free pore volume, which is the volume of the probe molecule probed, unit is Å³. V_0 is the occupied volume, which is the volume surrounded by the Connolly surface, unit is Å³.

As illustrated in Table 3 and Fig. 17, the porosity ranking from high to low is as follows: quartz > calcite > feldspar > chlorite > illite > kaolinite > montmorillonite. The overall trend indicates that the porosity of non-clay minerals was higher than that of clay minerals, leading to a large adsorption space for shale gas when non-clay minerals were present. Shale occurs primarily in two forms: free and adsorbed gas forms. The interactions between pore surfaces and gas molecules on the surface of organic matter leads to

the accumulation of gas molecules, forming an adsorbed phase. Therefore, higher porosity corresponds to a higher capacity for adsorbing gas molecules, leading to increased adsorption capacity.

5.2. Energy analysis

The density distribution curve demonstrated that methane molecules were adsorbed within the kerogen molecules. For the composite model, a minority of methane molecules was distributed on the surface of inorganic minerals. The results from adsorption enthalpy indicated that the entire adsorption process primarily involved physical adsorption, driven by the combined action of van der Waals and electrostatic forces, representing the adsorption of methane molecules on kerogen and inorganic mineral surfaces (Bhatia and Nicholson, 2012).

Table 4 presents the energy distribution in the single kerogen system under different temperature and pressure conditions. Under constant pressure, the van der Waals energy, as simulated by kinetic modeling, increased significantly with rising temperatures. The absolute value exhibited an initial decrease, followed by gradual increase. This phenomenon was attributed to the transition from releasing to absorbing van der Waals energy as the temperature increased (Chen et al., 2023b). The increasing absorption of van der Waals energy indicated a decrease in system stability. Furthermore, at constant temperature conditions, the increase in pressure led to a relatively minimal change in van der Waals energy, suggesting a substantial impact of temperature on the variation in van der Waals energy during methane adsorption. In addition, during methane adsorption in the mono kerogen system, the electrostatic energy exhibited a negative value, indicating the release of electrostatic energy by the system. The absolute value of this energy increased with pressure, highlighting an augmentation in the released energy and enhancement of the system's structural stability. Simultaneously, under the same pressure conditions, with increasing temperature, the electrostatic energy initially decreased and then increased, implying a corresponding decrease and subsequent increase in the released energy. These variations exhibited minor changes in amplitude, verifying that pressure significantly affected the alterations in classical energy (Zhou et al., 2023).

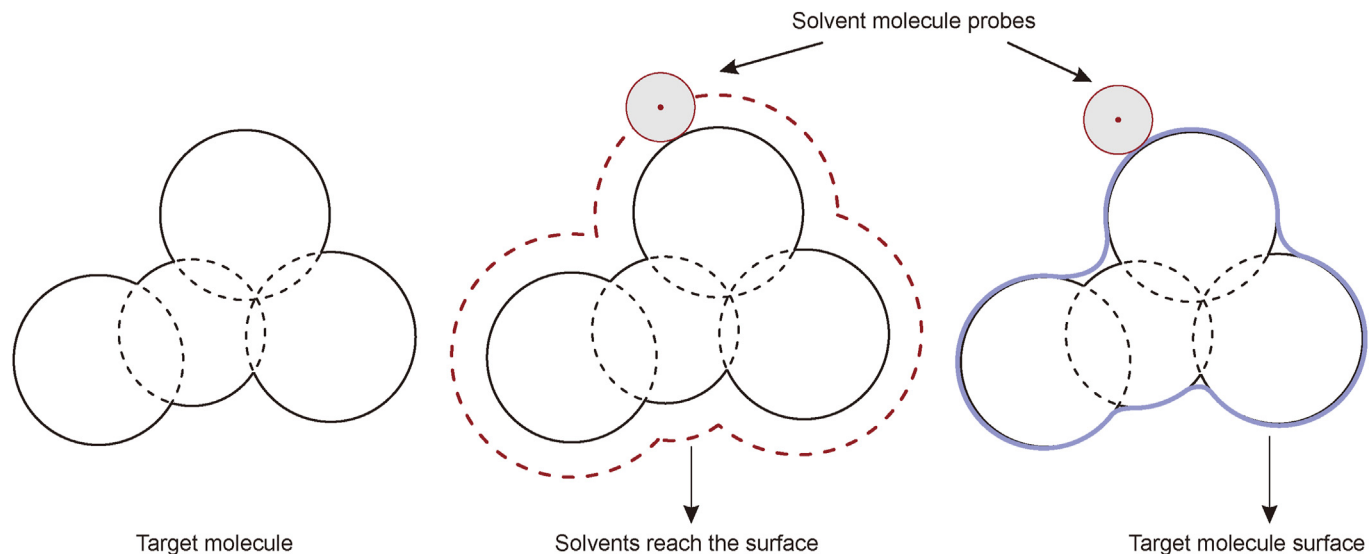


Fig. 16. Schematic diagram of Connolly molecular surface calculations (Revised according to (Yang et al., 2017)).

Table 3

Porosity of different shale composite systems.

System type	Kaolinite	Montmorillonite	Illite	Chlorite	Calcite	Quartz	Feldspar
Free pore volume, Å	30859.99	30374.56	35317.18	35762.57	37712.18	38511.88	34146.68
Occupieds volume, Å	57370.33	63565.91	63523.35	62851.97	58620.9	54282.09	56780.98
Porosity, %	34.98	32.33	35.73	36.26	39.15	41.50	37.55

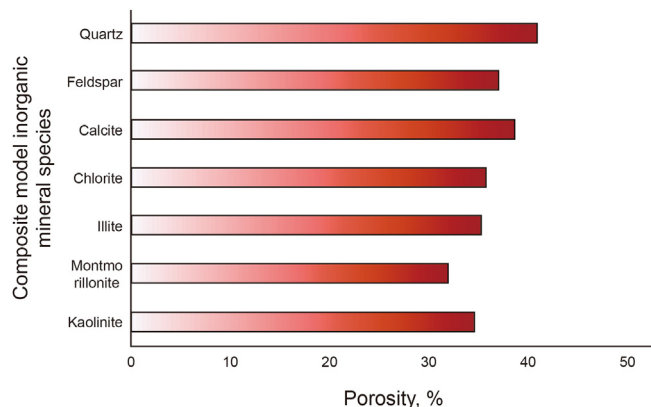


Fig. 17. Porosity of different shale composite systems.

5.3. Geological implications

Comparing the effects of inorganic matter and organic matter on the adsorption capacity of the composite model, as shown in Fig. 10(b)–(c), the organic matter plays a dominant role in the

adsorption of gases. The gases are primarily contained in the micropores of organic matter, as well as in the gap between organic matter and inorganic non-clay, and between gap between organic matter and inorganic clay minerals. This predominance can be attributed to the overall Poisson distribution of adsorption energy for different mineral composite model systems, with the non-clay mineral composite model positioned predominantly on the left side of the clay–mineral composite model (Fig. 12(c)–(d)). This result indicates that the adsorption capacity of the clay–mineral composite model is lower than that of the non-clay mineral composite model. The adsorption capacity of pure clay minerals for methane is stronger than that of non-clay minerals. However, compared to organic matter, the influence of inorganic minerals on methane adsorption capacity is minimal. In the inorganic mineral–kerogen organic matter composite system, the addition of inorganic minerals alters the porosity and adsorption mechanisms of the system. The porosity of quartz–organic matter composite models is higher than that of general clay mineral composite models. Additionally, quartz, as a rigid mineral, forms a sturdy framework that can partially protect primary interparticle pores from being completely destroyed. This provides stronger protection for adsorbed shale gas and offers significant storage space for shale gas, particularly for free gas (Li, 2023; Guan et al., 2021). The

Table 4

Energy distribution of single kerogen system under different temperature and pressure conditions.

Temperature, K	Van der Waals, kcal/mol	Electrostatic, kcal/mol	Pressure, MPa	Van der Waals, kcal/mol	Electrostatic, kcal/mol
Under the same pressure conditions					
298	-147.937	-36.607	5	189.655	-16.370
328	-37.973	-28.912	10	208.379	-19.065
358	224.493	-28.909	15	224.493	-28.909
388	458.672	-29.897	20	197.812	-40.384
418	723.825	-33.014	25	217.063	-59.775

Table 5

The change value of methane adsorption capacity under the same change of burial depth, pressure change and temperature change.

Temperature, K	Adsorption capacity, mmol/g	Pressure, MPa	Adsorption capacity, mmol/g
298	0.69762	5	7.09938
328	1.03104	10	6.56491
358	0.47669	15	6.89196
388	0.88527	20	6.57316
418	0.37057	25	6.1406

presence of inorganic non-clay makes the composite model more abundant, with greater resource potential, and is more brittle. This characteristic makes it more conducive to fracturing, thereby facilitating the formation of sweet spot areas for shale gas exploration and development.

In oil-bearing basins, as burial depth increases, temperature and pressure typically exhibited a gradual upward trend, which was conducive to the cracking of kerogen and the conversion of crude oil into gas. With increasing temperature, the adsorption capacity decreases, whereas the effect of pressure on the adsorption capacity gradually increases with pressure (Fig. 10(a)). This phenomenon is primarily attributed to methane adsorption shifting from lower energy adsorption sites to higher energy sites as pressure increases (Fig. 12(a)). Taking the Longmaxi Formation in the Sichuan Basin as an example, the geothermal gradient was 32.55–37.55 °C/km (Yang et al., 2019) and the pressure gradient was 16.7–21.7 kPa/m (Wang et al., 2023). For ease of calculation, the geothermal gradient was considered as 35 °C/km and the pressure gradient was 20 kPa/m. As shown in Table 5, when the pressure change is 20 MPa, the corresponding buried depth increases by 1 km, and the average adsorption capacity is 6.654 mmol/g. When the temperature change is 35 °C, corresponding to a 1 km increase in burial depth, with an average value of 0.692 mmol/g. Compared to the influence of temperature, the effect of pressure on methane adsorption was significantly greater at the same burial depth, which was approximately 9.62 times stronger. Consequently, the shale gas content that could be deposited at deep depth was greater, indicating higher resource potential.

In summary, shale formations with high organic matter content in the deep layer, high content of non-clay inorganic minerals, and increased temperature and pressure compared to shallow layers could host more shale gas. Therefore, deep shale gas was a favorable area for future exploration and development. The Wufeng Formation and Longmaxi Formation were the main target intervals for marine shale gas exploration and development in this area. These formations were dominated by black organic-rich siliceous shale (Wang et al., 2021b), with a high content of quartz minerals, which was conducive to the occurrence of shale gas. This study revealed the distribution and enrichment mechanism of shale gas in the Longmaxi Formation of Sichuan Basin from a microscopic perspective. These findings provide theoretical support for enhancing the recovery rate of deep shale gas and offer guidance for the exploration of deep shale gas in other basins.

6. Conclusions

In the mono kerogen system, methane adsorption capacity decreased with increasing temperature and increased with pressure. This phenomenon was primarily attributed to the weakening of interactions between methane and kerogen molecules in the system as the temperature rises. During the adsorption process, a significant amount of adsorption heat and energy was released, leading to a reduction in the system's energy and an increased in

stability. Consequently, the adsorption process became more favorable, resulting in an increased capacity for methane adsorption at increased temperatures. Moreover, methane molecules exhibited the strongest interaction forces with C atoms within the kerogen molecules, followed by the S atoms. Methane distribution within the kerogen nanopores primarily occurred within the pores of the kerogen polymer, concentrated at the center of the slit, along with methane molecules existing in a free state. In the adsorption process for the mono-kerogen system, the overall behavior was influenced by van der Waals and electrostatic forces. When there were substantial changes in temperature, the adsorption process was predominantly influenced by van der Waals forces. Conversely, when there were considerable variations in pressure, the system was substantially affected by electrostatic forces.

In the kerogen–mineral composite system, variations in the porosity of simulated shale models resulted in differing adsorption capacities and affinities across various mineral–shale composite models. The effect was particularly evident when comparing non-clay minerals to clay minerals considering their influence on methane adsorption by kerogen. Specifically, non-clay minerals enhanced the adsorption of methane by kerogen. Among these, quartz and calcite composite models demonstrated higher adsorption capacities than other mineral composite models, while montmorillonite composite models exhibited relatively lower adsorption capabilities. These results aligned with the magnitude of porosity, indicating that the addition of inorganic minerals can affect the overall porosity of the simulated shale system. In addition, the adsorption capacity of different kerogen–mineral composite systems were linked with the porosity of the system models. Higher porosity corresponded to a larger volume available for gas adsorption, thereby resulting in increased adsorption capability. In addition, in the context of methane adsorption in composite models, the organic components of kerogen predominantly governed the process, while the impact of inorganic minerals on methane adsorption in the system was relatively small.

The presence of inorganic non-clay minerals had a significant effect on the methane adsorption capacity of organic matter compared to inorganic clay minerals. At the same burial depth, the influence of increased pressure on methane adsorption was more pronounced than that of increased temperature. Consequently, deep shale formations can contain more shale gas, indicating greater resource potential. Thus, deep shale gas represents a favorable area for future exploration and development.

CRediT authorship contribution statement

Yu-Ying Wang: Writing – review & editing, Writing – original draft, Methodology, Conceptualization. **Jun-Qing Chen:** Writing – review & editing, Writing – original draft, Resources, Conceptualization. **Fu-Jie Jiang:** Writing – review & editing, Validation, Investigation, Data curation. **Xiao-Bin Yang:** Writing – review & editing, Formal analysis, Data curation, Conceptualization. **Xiao Zhang:** Project administration, Methodology, Funding acquisition. **Hong Pang:** Writing – review & editing, Methodology, Formal analysis, Data curation, Conceptualization. **Dong-Xia Chen:** Resources, Methodology, Formal analysis. **Bing-Yao Li:** Software, Methodology, Funding acquisition. **Xin-Yi Niu:** Visualization, Software. **Gui-Li Ma:** Visualization, Software. **Kan-Yuan Shi:** Visualization, Software.

Declaration of competing interest

The authors declare that they have no known competing financial interests or personal relationships that could have appeared to influence the work reported in this paper.

Acknowledgments

This research was supported by the National Natural Science Foundation of China, (Grant No. 42102145), the Science Foundation of China University of Petroleum, Beijing (Grant No. 2462022YXZZ007).

References

- Alberto, V., Alessandro, F., Gualtieri, Gilberto, A., 2015. The nature of disorder in montmorillonite by simulation of X-ray powder patterns. *Am. Mineral.* (7). <https://doi.org/10.1515/am-2002-0720>.
- Ambrose, R.J., Clarkson, C.R., Youngblood, J., Adams, R., Nguyen, P., Nobakht, M., Biseda, B., 2011. Life-cycle decline curve estimation for tight/shale reservoirs. The SPE Hydraulic Fracturing Technology Conference. <https://doi.org/10.2118/140519-MS>. January, 2011.
- Antao, S.M., Ishmael, H., Wang, J., Peter, L.L., Brian, H.T., 2008. State-of-the-art high-resolution powder x-ray diffraction (hrpxrd) illustrated with rietveld structure refinement of quartz, sodalite, tremolite, and meionite. *Can. Mineral.* 46 (6), 1501–1509. <https://doi.org/10.3749/canmin.46.5.1501>.
- Bhatia, S.K., Nicholson, D., 2012. Adsorption and diffusion of methane in silica nanopores: a comparison of single-site and five-site models. *J. Phys. Chem.* 116 (3), 2344–2355. <https://doi.org/10.1021/jp210593d>.
- Bish, D.L., 1993. Rietveld refinement of the kaolinite structure at 1.5 K. *Clays Clay Miner.* 41 (6), 738–744.
- Chen, L., Huang, D.B., Li, Z.Z., He, Y.L., Tao, W.Q., 2016. Study on methane adsorption in graphite slit-pores by molecular dynamics simulation. *Therm. Sci. Technol.* 15 (2), 92–96. <https://doi.org/10.13738/j.issn.1671-8097.2016.02.002>.
- Chen, S.B., Han, Y.F., Fu, C.Q., Zhang, H., Zhu, Y.M., Zuo, Z.X., 2023a. Micro and nano-size pores of clay minerals in shale reservoirs: Implication for the accumulation of shale gas. *Sediment. Geol.* 342 (1), 180–190. <https://doi.org/10.1016/j.sedgeo.2016.06.022>.
- Chen, C., Hu, W.F., Sun, J.Y., Li, W.Z., Song, Y.C., 2019. CH₄ adsorption and diffusion in shale pores from molecular simulation and a model for CH₄ adsorption in shale matrix. *Int. J. Heat Mass Tran.* 141, 367–378. <https://doi.org/10.1016/j.ijheatmasstransfer.2019.06.087>.
- Chen, J.Q., Jiang, F.J., Cong, Q., Pang, X.Q., Ma, K.Y., Shi, K.Y., Pang, B., Chen, D.X., Pang, H., Yang, X.B., Wang, Y.Y., Li, B.Y., 2023b. Adsorption characteristics of shale gas in organic-inorganic slit pores. *Energy* 2023, 278. <https://doi.org/10.1016/j.energy.2023.127788>.
- Cong, Q., 2023. Molecular Dynamics Simulation of Main Controlling Factors and Microscopic Mechanism of Continental Shale Gas Adsorption. China University of Petroleum, Beijing. <https://doi.org/10.27643/d.cnki.gsybu.2023.002013>.
- Cong, Q., Chen, J.Q., Lu, G.W., Jiang, F.J., Pang, B., Shi, K.Y., Yang, X.B., Wang, Y.Y., Pang, H., 2022. Review on influencing factors and microscopic mechanism of shale adsorption capacity by molecular dynamics simulation. *J. Cent. S. Univ.* 53 (9), 3474–3489.
- Connolly, M.L., 1983. Solvent-accessible surfaces of proteins and nucleic acids. *Science*. Aug 19 (4612), 709–713. <https://doi.org/10.1126/science.6879170>, 221.
- Curtis, J.B., 2002. Fractured shale-gas systems. AAPG (Am. Assoc. Pet. Geol.) Bull. 86 (1), 1921–1938. <https://doi.org/10.1306/61EEDDBE-173E-11D7-8645000102C1865D>.
- Dawn, L., Geatches, Jennifer, W., 2014. Ab initio investigations of dioctahedral interlayer-deficient mica: modelling 1M polymorphs of illite found within gas shale. *Eur. J. Mineral.* 26 (10), 127–144. <https://doi.org/10.1127/0935-1221/2013/0025-2352>.
- Elbashier, E., Hussein, I., Carchini, G., Kasha, A., Berdiyorov, G., 2021. Influence of natural gas composition on adsorption in calcite nanopores: a dft study. *Appl. Surf. Sci.* 568, 150940. <https://doi.org/10.1016/j.apsusc.2021.150940>.
- Fang, R.H., Liu, X.Q., Zhang, C., Li, M.J., Xia, X.H., Huang, Z.L., Yang, C.Y., Han, Q.Y., Tang, H.Q., 2022. Molecular simulation of shale gas adsorption under temperature-pressure coupling: a case study of the Lower Cambrian in western Hubei region. *Nat. Gas Geosci.* 33 (1), 138–152.
- Gensterblum, Y., Merkel, A., Busch, A., Krooss, B.M., 2013. High-pressure CH₄ and CO₂ sorption isotherms as a function of coal maturity and the influence of moisture. *Int. J. Coal Geol.* 118, 45–57. <https://doi.org/10.1016/j.jcoal2013.07.024>.
- Gong, F.M., Hou, D.L., Qiang, X.Y., Xiang, X.N., Huang, S.J., Han, X., Yu, Y.Y., Gu, K.F., 2024. CH₄-CO₂ competitive adsorption and CO₂ sequestration in Na-montmorillonite silt. In: Journal of Jilin University, 54. (Earth Science Edition), pp. 470–478. <https://doi.org/10.13278/j.cnki.jjuese.20220230> (2) (in Chinese).
- Guan, Q.Z., Dong, D.Z., Zhang, H.L., Sun, S.S., Zhang, S.R., Guo, W., 2021. Types of biogenic quartz and its coupling storage mechanism in organic-rich shales: a case study of the upper ordovician wufeng formation to lower silurian Longmaxi Formation in the Sichuan Basin, SW China. *Petrol. Explor. Dev.* 48 (4), 700–709.
- Hao, Y., Xu, H.Y., Fan, J.C., Zhu, Y.B., Wang, F.C., Wu, H.A., 2020. Transport of shale gas in microporous/nanoporous media: molecular to pore-scale simulations. *Energy Fuel.* 35 (2), 911–943. <https://doi.org/10.1021/acs.energyfuels.0c03276>.
- Hou, D.L., Han, X., Tang, H.M., Guo, J.C., Gong, F.M., Sun, L., Qiang, X.Y., 2023. Primary research on expression of kerogen in Longmaxi shale and its adsorption characteristics. *Petrol. Res. Evaluat. Dev.* 13 (5), 636–646.
- Huang, L., 2020. Research on Multi-Component Competitive Adsorption Mechanism of Shale Gas Based on Molecular Simulation. China University of Petroleum (Beijing). <https://doi.org/10.27643/d.cnki.gsybu.2020.000077>.
- Huang, L., Ning, Z.F., Wang, Q., Qi, R.R., Zeng, Y., Qin, H.B., Ye, H.T., Zhang, W.T., 2017. Molecular simulation of adsorption behaviors of methane, carbon dioxide and their mixtures on kerogen: effect of kerogen maturity and moisture content. *Fuel*. <https://doi.org/10.1016/j.fuel.2017.09.060>.
- Jia, T.G., Wu, X.Y., Qu, G.N., 2023. Molecular simulation of thermodynamic properties of CH₄/CO₂ adsorption by coal molecules at different temperatures and moisture contents under variable pressure conditions. *ACS Omega* 8 (50), 48381–48393. <https://doi.org/10.1021/acsomega.3c07872>.
- Katti, D.R., Thapa, K.B., Katti, K.S., 2017. Modeling molecular interactions of sodium montmorillonite clay with 3D kerogen models. *Fuel* 199, 641–652. <https://doi.org/10.1016/j.fuel.2017.03.021>.
- Li, N., 2020. Molecular simulation study on gas adsorption, diffusion and displacement characteristics in composite shale. *Chin. Univ. Petrol.* <https://doi.org/10.27644/d.cnki.gsydu.2020.0001625>.
- Li, M., 2023. Evolution Model of Shale Gas Occurrence State and Gas-bearing Property Evaluation in Longmaxi Formation of Sichuan Basin. China University of Petroleum, Beijing. <https://doi.org/10.27643/d.cnki.gsybu.2023.001520>.
- Li, N., Ding, B., Gu, Z.K., Gong, L., 2021. Molecular simulation of competitive adsorption characteristics of gases in different composite shale models. *Therm. Sci. Technol.* 20 (4), 380–385. <https://doi.org/10.13738/j.issn.1671-8097.202024>.
- Li, J.H., Han, X., Huang, S.J., Yu, Y.Y., Qiang, X.Y., Gu, K.F., Hou, Dali, 2022. Molecular simulation of kerogen adsorption law in shale. *Reser. Evaluat. Dev.* 12 (3), 455–461. <https://doi.org/10.13809/j.cnki.cn32-1825/te.2022.03.007>.
- Liu, B., Shi, J.Q., Shen, Y., Zhang, J., 2013. A molecular dynamics simulation of methane adsorption in graphite slits. *Computat. Phys.* 30 (5), 692–699. <https://doi.org/10.19596/j.cnki.1001-246x.2013.05.008>.
- Liu, X.Q., He, X., Qiu, N.X., Yang, X., Tian, Z.Y., Li, M.J., Xue, Y., 2016. Molecular simulation of CH₄, CO₂, H₂O and N₂ molecules adsorption on heterogeneous surface models of coal. *Appl. Surf. Sci.* 389, 894–905. <https://doi.org/10.1016/j.apsusc.2016.08.021>.
- Liu, X.J., Luo, D.X., Xiong, J., Liang, L.X., 2017. Construction of the average molecular modeling of the kerogen from the Longmaxi formation. *Chem. Eng. Prog. Sci.* 36 (2), 530–537. <https://doi.org/10.16085/j.issn.1000-6613.2017.02.019>.
- Liu, J.Y., Wen, Y.M., Yuan, H., Jiang, L., Liu, Z.B., Chen, Y.Z., Shui, Z.W., 2023. Molecular simulation calculation method for shale gas adsorption in realistic shale model. *Geoenergy Sci. Eng.* 222, 211440. <https://doi.org/10.1016/j.GEOEN.2023.211440>.
- Markgraf, S.A., Richard, J., Reeder, 1985. High-temperature structure refinements of calcite and magnesite. *Am. Mineral.* 70 (5–6), 590–600.
- Nan, Y.L., Li, W.H., Jin, Z.H., 2020. Slip length of methane flow under shale reservoir conditions: effect of pore size and pressure. *Fuel* 259, 116237. <https://doi.org/10.1016/j.fuel.2019.116237>.
- Pan, N., Zhao, D.F., Wei, Y., Jiao, W.W., Wei, H., 2022. Characteristics of deep shale minerals in Longmaxi Formation in western Chongqing and their reservoir geological significance. *Unconvent. Oil Gas* 9 (2), 8–14+33. <https://doi.org/10.19901/j.fcgqy.2022.02.02>.
- Pang, W.Y., He, Y.Q., Yan, C.H., Jin, Z.H., 2019. Tackling the challenges in the estimation of methane absolute adsorption in kerogen nanoporous media from molecular and analytical approaches. *Fuel* 242, 687–698. <https://doi.org/10.1016/j.fuel.2019.01.059>.
- Piera, B., Mario, T., Emiliano, B., 1999. High-temperature in situ structural investigation on lead feldspar. *Am. Mineral.* 84 (1–2), 120–129. <https://doi.org/10.2138/am-1999-1-213>.
- Shi, X.W., Zhou, S.W., Tian, C., Li, D., Li, D.Y., Li, Y., Wu, W., Cai, C.H., Chen, Y.L., 2021. Methane adsorption characteristics and controlling factors of deep shale gas in southern Sichuan Basin, China. *Nat. Gas Geosci.* 32 (11), 1735–1747.
- Shi, K.Y., Chen, J.Q., Pang, X.Q., et al., 2023. Wettability of different clay mineral surfaces in shale: implications from molecular dynamics simulations. *Pet. Sci.* 20 (2), 689–704. <https://doi.org/10.1016/j.petsci.2023.02.001>.
- Shi, K.Y., Chen, J.Q., Pang, X.Q., Jiang, F.J., Hui, S.S., Zhang, S.J., Pang, H., Wang, Y.Y., Chen, D., Yang, X.B., Li, B.Y., Pu, T.Y., 2024. Average molecular structure model of shale kerogen: experimental characterization, structural reconstruction, and pyrolysis analysis. *Fuel* 355, 129474. <https://doi.org/10.1016/j.fuel.2023.129474>.
- Stryjek, Roman, Juan, H.V., 1986. PRSV: an improved peng-robinson equation of state for pure compounds and mixtures. *Can. J. Chem. Eng.* 64, 323–333. <https://doi.org/10.1002/cjce.5450640224>.
- Sudibandriyo, M., Pan, Z.J., Fitzgerald, J.E., Robinson, R.L., Gasem, K.A., 2003. Adsorption of methane, nitrogen, carbon dioxide, and their binary mixtures on dry activated carbon at 318.2 K and pressures up to 13.6 MPa. *Langmuir* 19 (13), 5323–5331. <https://doi.org/10.1021/la020976k>.
- Sun, H.Y., Zhao, H.Q., Qi, N., Li, Y., 2017. Molecular insights into the enhanced shale gas recovery by carbon dioxide in kerogen slit nanopores. *J. Phys. Chem. C* 121 (18), 10233–10241. <https://doi.org/10.1021/acs.jpcc.7b02618>.
- Tissot, B., Durand, B., Espitalié, J., Combaz, A., 1974. Influence of nature and diagenesis of organic matter in Formation of petroleum. AAPG (Am. Assoc. Pet. Geol.) Bull. 58 (3), 499–506. <https://doi.org/10.1306/83D91425-16C7-11D7-8645000102C1865D>.
- Wang, S., Feng, Q.H., Zha, M., Lu, S.F., Qin, Y., Xia, T., Zhang, C., 2015. Molecular dynamics simulation of liquid alkane occurrence state in pores and slits of shale organic matter. *Petrol. Explor. Dev. Online*. Dec 42 (6), 844–851. [https://doi.org/10.1016/S1876-3804\(15\)30081-1](https://doi.org/10.1016/S1876-3804(15)30081-1).
- Wang, S., Feng, Q.H., Zha, M., Farzam, J., Hu, Q.H., 2017. Supercritical methane diffusion in shale nanopores: effects of pressure, mineral types, and moisture content. *Energy Fuel.* 32 (1), 169–180. <https://doi.org/10.1021/acs.energy-fuels.7b02892>, 2018.

- Wang, T.Y., Tian, S.C., Li, G.S., Tian, S.C., Li, G.S., Sheng, M., 2018. Selective adsorption of supercritical carbon dioxide and methane binary mixture in shale kerogen nanopores. *J. Nat. Gas Sci. Eng.* 50, 181–188. <https://doi.org/10.1016/j.jngse.2017.12.002>.
- Wang, X.H., Huang, X.F., Lin, K., Zhao, Y.P., 2019. The constructions and pyrolysis of 3D kerogen macromolecular models: experiments and simulations. *Global Challenges* 3 (5), 1900006. <https://doi.org/10.1002/gch2.201900006>.
- Wang, Y., Yang, H.L., Huang, H.Y., Fu, L., Chen, G., Zhang, H., Wang, Z.X., Guo, K.J., 2023. Research and application of deep shale gas geomechanics in Lu zhou block, Sichuan Basin. *Chin. Petrol. Explorat.* 28 (5), 68–83.
- Wang, J., Tang, J., Chen, F., 2024b. Methane adsorption and transport in tortuous slit-like nanochannels: a molecular simulation study. *ACS Omega* 9 (42), 43093–43105. <https://doi.org/10.1021/ACSM/OMEGA.4C06969>.
- Wang, R.Y., Hu, Z.Q., Bao, H.Y., Wu, J., Du, W., Wang, P.W., Peng, Z.Y., Lu, T., 2021. Diagenetic evolution of key minerals in shale from upper ordovician Wu feng Formation-lower silurian Longmaxi Formation in Sichuan Basin and its storage control. *Petrol. Geol. Experiment* 43 (6), 996–1005.
- Wang, J., Hu, S., Yang, T., Chen, X.H., Li, W.P., Wang, T., 2024a. Mechanistic study of carbon dioxide sequestration technology using molecular simulations to assess the adsorption of methane and carbon dioxide by different functional groups. *Appl. Surf. Sci.* 677, 161058. <https://doi.org/10.1016/JAPSUSC.2024.161058>.
- Wang, R., Yang, C.X., Ru, H.Y., Wang, P., Yang, Y., 2021. Comparison of error in methane isotherm adsorption by volumetric method for shale and coal. *Unconvent. Oil Gas* 8 (3), 43–48.
- Xu, C.X., Xue, H.T., Li, B.H., Lu, S.F., Zhang, J., Chen, G.H., Wang, S., 2020. Microscopic adsorption mechanism difference in the mineral pore of shale gas reservoir. *Special Oil Gas Reservoirs* 27 (4), 79–84.
- Yan, J., Zang, T.W., Li, Y., Lv, H.G., Zhang, X., 2013. Effect of the organic matter characteristics on methane adsorption in shale. *J. China Coal Soc.* 38 (5), 805–811.
- Yang, L., Li, M.J., Liu, X.Q., Jiang, W.D., Yang, C.Y., Lai, H.F., Kang, P., 2017. Using Connolly surface to characterize the adsorption of methyldibenzothiophenes, and their chemical mechanism as molecular tracer for oil filling pathways. *Geochemistry* 46 (4), 367–372. <https://doi.org/10.19700/j.0379-1726.2017.04.007>.
- Yang, P., Wang, Z.J., Yu, Q., Liu, W., Liu, J.H., Xiong, G.Q., He, J.L., Yang, F., 2019. An resources potential analysis of Wufeng-Longmaxi Formation shale gas in the southwestern margin of Sichuan Basin. *Chin. Geol.* 46 (3), 601–614.
- Yuan, S., Gang, H.Z., Zhou, L., Liang, T.T., Irfan, M., Kazmi, M., Liu, J.F., Yang, S.Z., Mu, B.Z., 2020. Insight into the adsorption mechanisms of CO₂, CH₄, and their mixtures on kerogen type IIIA. *Energy Fuel* 34 (11), 14300–14311. <https://doi.org/10.1021/acs.energyfuels.0c01368>.
- Zanazzi, P.F., Montagnoli, M., Nazzareni, S., Comodi, P., 2007. Structural effects of pressure on monoclinic chlorite: a single-crystal study. *Am. Mineral.* 92 (4), 655–661. <https://doi.org/10.2138/am.2007.2341>.
- Zeng, K.C., Jiang, P.X., Lun, Z.M., Xu, R.N., 2018. Molecular simulation of carbon dioxide and methane adsorption in shale organic nanopores. *Energy Fuel* 33 (3), 1785–1796. <https://doi.org/10.1021/acs.energyfuels.8b02851>.
- Zhang, D.X., 2013. An overview of shale gas production. *Acta Petrol. Sin.* 34 (4), 792–801.
- Zhang, T.W., Ellis, G.S., Ruppel, S.C., Milliken, K., Yang, R.S., 2012. Effect of organic matter type and thermal maturity on methane adsorption in shale-gas systems. *Organic Geochem.* 47, 120–131. <https://doi.org/10.1016/j.orggeochem.2012.03.012>.
- Zhang, J.F., Clennell, M.B., Dewhurst, D.N., Liu, K.Y., 2014. Combined Monte Carlo and molecular dynamics simulation of methane adsorption on dry and moist coal. *Fuel* 122, 186–197. <https://doi.org/10.1016/j.fuel.2014.01.006>. ISSN 0016-2361.
- Zhou, B., Zhou, Z.D., Zhou, Y., 2023. Diffusion/adsorption/dissolution coupling process of methane gas in kerogen nano-slit: molecular simulation and a chemical potential-based mass transfer model. *Chem. Phys. Lett.* 830, 140789. <https://doi.org/10.1016/j.cplett.2023.140789>.